

Quantification of dopaminergic neurotransmission SPECT studies with ^{123}I -labelled radioligands. A comparison between different imaging systems and data acquisition protocols using Monte Carlo simulation

Cristina Crespo · Judith Gallego · Albert Cot ·
Carles Falcón · Santiago Bullich · Deborah Pareto ·
Pablo Aguiar · Josep Sempau · Francisco Lomeña ·
Francisco Calviño · Javier Pavía · Domènec Ros

Received: 29 June 2007 / Accepted: 26 December 2007 / Published online: 12 March 2008
© Springer-Verlag 2008

Abstract

Purpose ^{123}I -labelled radioligands are commonly used for single-photon emission computed tomography (SPECT) imaging of the dopaminergic system to study the dopamine transporter binding. The aim of this work was to compare the quantitative capabilities of two different SPECT systems through Monte Carlo (MC) simulation.

Methods The SimSET MC code was employed to generate simulated projections of a numerical phantom for two gamma cameras equipped with a parallel and a fan-beam collimator, respectively. A fully 3D iterative reconstruction algorithm was used to compensate for attenuation, the spatially variant point spread function (PSF) and scatter. A

post-reconstruction partial volume effect (PVE) compensation was also developed.

Results For both systems, the correction for all degradations and PVE compensation resulted in recovery factors of the theoretical specific uptake ratio (SUR) close to 100%. For a SUR value of 4, the recovered SUR for the parallel imaging system was 33% for a reconstruction without corrections (OSEM), 45% for a reconstruction with attenuation correction (OSEM-A), 56% for a 3D reconstruction with attenuation and PSF corrections (OSEM-AP), 68% for OSEM-AP with scatter correction (OSEM-APS) and 97% for OSEM-APS plus PVE compensation (OSEM-APSV). For the fan-beam imaging system, the recovered SUR was 41% without

C. Crespo · A. Cot · C. Falcón · P. Aguiar · D. Ros (✉)
Unitat de Biofísica i Bioenginyeria, Departament de Ciències
Fisiològiques I, Facultat de Medicina,
Universitat de Barcelona—IDIBAPS,
Casanova 143,
08036 Barcelona, Spain
e-mail: dros@ub.edu

J. Gallego · J. Sempau · F. Calviño
Institut de Tècniques Energètiques, Universitat Politècnica de
Catalunya,
Barcelona, Spain

J. Gallego
Institut de Bioenginyeria de Catalunya,
Barcelona, Spain

A. Cot · F. Calviño
Secció d'Enginyeria Nuclear, Departament de Física i Enginyeria
Nuclear, Universitat Politècnica de Catalunya,
Barcelona, Spain

C. Falcón · D. Pareto · J. Sempau · J. Pavía · D. Ros
CIBER en Bioenginyeria, Biomateriales y Nanomedicina
(CIBER-BBN),
Barcelona, Spain

S. Bullich
Center for Imaging in Psychiatry, CRC-MAR, Hospital del Mar,
Barcelona, Spain

D. Pareto
Institut d'Alta Tecnologia, PRBB,
Barcelona, Spain

F. Lomeña · J. Pavía
Servei de Medicina Nuclear, Hospital Clínic, IDIBAPS,
Barcelona, Spain

corrections, 55% for OSEM-A, 65% for OSEM-AP, 75% for OSEM-APS and 102% for OSEM-APSV.

Conclusion Our findings indicate that the correction for degradations increases the quantification accuracy, with PVE compensation playing a major role in the SUR quantification. The proposed methodology allows us to reach similar SUR values for different SPECT systems, thereby allowing a reliable standardisation in multicentric studies.

Keywords Brain SPECT · Receptor imaging · SPECT instrumentation and algorithms · Monte Carlo methods · Reconstruction quantification

Introduction

Parkinson's disease is a neurological disorder associated with the loss of dopaminergic neurons from the substantia nigra and with an important dopamine depletion in the striatum [1]. A number of ^{123}I agents have been developed for single-photon emission computed tomography (SPECT) imaging of the dopaminergic system to study the presynaptic dopamine transporter (DAT) binding. Commercially available pharmaceuticals labelled with ^{123}I , such as β -2-carbomethoxy-3-(4'-iodophenyl)tropane (β -CIT) and fluoropropyl-CIT [2], have shown a high affinity for the DAT. Quantification of DAT SPECT imaging is suitable for discriminating Parkinsonian syndromes from other movement disorders, facilitating an early diagnosis of the disease [3], following up the progression of the disease [4–6] and for assessing the effects of treatment strategies [7].

To objectively assess striatal DAT binding, quantification is mandatory [8]. Nevertheless, the different degradations that are involved in the reconstruction process affect the quantification output. Thus, image-degrading effects such as attenuation, the spatially variant point spread function (PSF), scatter and the partial volume effect (PVE) have to be compensated to achieve an accurate quantification [9–13].

As regards to scatter, correction methods that model the three-dimensional (3D) scatter distribution through Monte Carlo (MC) simulation have been shown to perform an accurate quantification [14, 15]. We previously developed an absolute quantification method (AQM) for neurotransmission studies, which included a 3D iterative reconstruction algorithm with MC-based scatter compensation [12]. This method yielded good results in studies using $^{99\text{m}}\text{Tc}$ -labelled radioisotopes. However, in the ^{123}I decay scheme, there are a few high-energy photons that have a non-negligible contribution to the final image [13, 16]. The effect of this high-energy contamination has to be compensated to improve the image quality and quantification.

Generally, PVE causes an underestimation of activity [17]. This effect is especially severe in small structures such as the basal ganglia. Given its significance, PVE correction methods have been developed in parallel by a number of research groups [18–23].

Brain neurotransmission SPECT imaging with ^{123}I is often performed with low energy high resolution (LEHR) parallel and fan-beam collimators [8]. In this work, a quantitative comparison of two imaging systems equipped with a parallel and a fan-beam collimator that employ different data acquisition protocols is made. To this end, an extension of the previous AQM was developed to include a MC-based scatter compensation for the high-energy contamination. This updated reconstruction algorithm uses a modelling of the high-energy PSF (hPSF) to accelerate the MC simulation. A handy post-reconstruction PVE compensation was also performed. The AQM with post-reconstruction PVE correction was used to assess the differences in the quantitative estimates between brain SPECT studies. As the quantification results had to be evaluated to test their reliability and accuracy, MC simulations with numerical phantoms were employed. Ideally, this quantification method should result in similar quantification values for both imaging configurations after correcting for all the degradations.

Materials and methods

The quantification method designed was evaluated through MC projections simulated for the following two camera/collimator combinations: Siemens E.CAM with LEHR parallel-hole collimator and Elscint HELIX with LEHR fan-beam collimator.

Numerical Phantom

Simulated projections were generated by using a numerical phantom obtained from a CT scan of the anthropomorphic striatal brain phantom (Radiological Support Devices, Long Beach, CA). The CT scan image consisted of $256 \times 256 \times 196$ cubic voxels with a voxel size of $0.89 \times 0.89 \times 0.89 \text{ mm}^3$. Brain tissue and bone were automatically segmented by thresholding the CT image, while the striatal cavities were manually drawn over the corresponding slices.

The non-uniform attenuation map was obtained by setting the appropriate attenuation coefficients to brain and bone depending on the energy of the simulated photons. Thirty different activity distributions were considered. For all these distributions, a constant value of 14 kBq/mL was assigned to the brain tissue. The striatal nuclei had a variety of values ranging from 15 to 98 kBq/mL to simulate 30 random values of the specific uptake ratio (SUR), which

modelled normal and pathological distributions. SUR was defined as:

$$\text{SUR} = \frac{\overline{A_s} - \overline{A_o}}{\overline{A_o}} \quad (1)$$

where $\overline{A_s}$ is the mean activity concentration in the striatal region and $\overline{A_o}$ is the mean activity concentration in a reference region located in the occipital area. Figure 1 shows one section of the activity distribution and the attenuation map used in the simulations.

SimSET simulation

The SimSET MC code [24] was employed to simulate the SPECT projections. ^{123}I photons with 159 keV (low-energy) and gamma-rays with higher energies (high-energy) were simulated separately and, finally, added together to obtain the total projections. For each camera/collimator system, the PSFs for the low-energy photons were calculated using the Gaussian function derived in [25], while the high-energy contamination effect was modelled using the hPSFs as described in [26]. These PSFs and hPSFs were included in SimSET to adapt the code to the ^{123}I -labelled radioligands simulation case. Table 1 summarises the simulation parameters used for both imaging systems. The differences in the setting that can be observed in Table 1 are due to the different acquisition protocols used for each gamma camera. Energy windows were selected according to the values proposed by the manufacturers.

A total of 30 noisy projections for each SPECT gamma camera were generated by employing the randomly distributed values of SUR ranging from 0.1 to 6. All the simulated studies were considered to have approximately 3 million counts, thus mimicking real studies obtained with these two imaging systems.



Fig. 1 A central slice of the activity distribution (*left*) and the attenuation map (*right*) of the striatal phantom. The striatal nuclei can be observed in the activity distribution

Table 1 Simulation parameters used for both SPECT systems

	System	
	E.CAM	HELIX
Collimator	LEHR parallel-hole	LEHR fan-beam
Focal length (mm)	NA	355
Hole shape	Hexagonal	Hexagonal
Hole radius (mm)	0.641	0.866
Septal thickness (mm)	0.16	0.20
Length (mm)	24.05	40.00
Number of projections	128	120
Matrix size	128 × 128	128 × 128
Bin size (mm)	3.900	4.424
Energy window (%)	15	20
Radius (mm)	150	150

Reconstruction algorithm

The AQM consists of a 3D iterative reconstruction algorithm based on the ordered subsets expectation maximisation (OSEM) algorithm [27], which includes a MC-based simulator as a forward projector for modelling the scatter component. The voxel values λ_i are updated in each step of the reconstruction process using the expression [12–14, 28]:

$$\lambda_i^{k+1} = \frac{\lambda_i^k}{\sum_{j=1}^{\text{nbins}} t_{ji}} \sum_{j=1}^{\text{nbins}} \frac{t_{ji} p_j}{\sum_{m=1}^{\text{nvox}} t_{jm} \lambda_m^k + s_j} \quad (2)$$

where p_j are the original projections, k is the iteration number, t_{ji} is the transition matrix and s_j is the scatter contribution estimated in bin j . The attenuation and the PSF are incorporated into the transition matrix, while the scatter contribution is calculated as:

$$s_j = s_j^{\text{LE}} + s_j^{\text{HE}} \quad (3)$$

where s_j^{LE} and s_j^{HE} are the low- and high-energy photons, which have mostly suffered scattering and have been finally detected. The scatter estimate s_j is calculated using the reconstructed image of the original projections without any scatter compensation. This image is the input activity distribution of the SimSET simulator weighted by the corresponding emission yields of each ray. Once the scatter distribution is estimated, it is replaced in Eq. 2 to generate the reconstructed image. One remarkable fact is that in the AQM, the scatter fraction is included in the forward projector, which means that the scatter correction does not remove counts from the original projections. As a consequence, noise is not increased after the scatter correction, which it is an advantage of the AQM over other scatter correction methods used in clinical routine.

As a result, the AQM provides an image that is corrected by attenuation, PSF and scatter. Table 2 summarises the reconstruction parameters used for each camera.

Given that the convergence of the reconstruction process is not the same for the two collimators, the number of iterations needed for each camera is different. As an objective criterion, an additional iteration was calculated whenever the recovered SUR values increased at least by 1%.

Projections had to be filtered with masks before reconstruction because of high-energy contamination. Thus, the values located outside the field of view of the phantom were discarded to prevent them from interfering in the reconstruction process. Masking was performed by applying a geometric projector to the attenuation map and giving a value of 1 inside the resulting projections and 0 outside their limits.

Quantification of striatal uptake ratio with PVE correction

The size of the volumes of interest, particularly for small volumes such as the caudate and putamen, has a direct impact on the measurement of the activity concentration. Thus, correction for PVE should be performed to obtain the accurate quantification of the striatal nuclei. An approach to correcting the PVE in neuroreceptor imaging has been described by Fleming et al. [29, 30]. In the present work, we extend their approach by using 3D regions of interest (ROIs). Thus, our methodology is essentially based on the measurement of the total activity in the striatum and on the calculation of the exact volume of interest for each region and study. In clinical studies, the striatal ROIs could be obtained by segmenting MRI images registered with the SPECT images. In this high-resolution space, the total activity in the striatum is calculated by using automatically expanded ROIs. These are large enough to ensure the inclusion of all the activity that has spread outside the physical volume of the structures because of PVE. The advantage of using an automatic expansion of these ROIs is a reduced operator-introduced variability in their positioning.

Table 2 Reconstruction parameters used for both SPECT systems

Parameter	System	
	E.CAM	HELIX
Pixel size (mm)	2.296	2.296
Slice thickness (mm)	3.900	4.424
Image size	128×128	128×128
Number of slices	45	40
Number of subsets	32	30
Transition matrix size per subset (MB)	481	493
Number of iterations	8	6
3D reconstruction time per SPECT study (h)	2	2

In this work, striatal and occipital ROIs were defined by using a CT image of the anthropomorphic striatal brain phantom. To perform the quantification of the studies, all reconstructed images were re-sampled to the high-resolution space where the ROIs were defined. The exact volumes of the ROIs were calculated using the 3D ROI map. Compensation for the PVE was carried out by expanding the original striatal ROI and calculating the mean activity concentration inside the expanded ROI. The total activity, A_s , inside the original striatal ROI was calculated by removing the non-specific uptake from the total activity in the expanded ROI:

$$A_s = \overline{A}_{s'}V_{s'} - \overline{A}_o(V_{s'} - V_s) \tag{4}$$

where $\overline{A}_{s'}$ and \overline{A}_o are, respectively, the mean activity concentrations inside the expanded striatal ROI and the occipital region and V_s and $V_{s'}$ are the volumes of the original and the expanded striatal ROI, respectively.

Taking into account that the mean activity concentration inside the original striatal ROI is defined as $\overline{A}_s = A_s/V_s$ and substituting Eq. 4 in Eq. 1, the SUR value after PVE correction can be calculated as:

$$SUR = \frac{(\overline{A}_{s'} - \overline{A}_o)V_{s'}}{\overline{A}_oV_s} \tag{5}$$

Note that this methodology assumes that the activity concentration of the background region is a good estimate of the non-specific uptake in the striatal ROI.

The expansion of the striatal ROI was established by calculating the resolution of the reconstruction method. This value was obtained by using SimSET to project a linear source in air with only low-energy photon emission and reconstructing the projections with PSF correction. The simulation and reconstruction were performed using the same parameters as those selected for the striatal phantom. The reconstructed image was fitted to a Gaussian function, and the standard deviation σ was calculated. Then, the striatal ROI was enlarged by 1σ . For the E.CAM parallel system, σ had a value of 1.90 mm (which leads to $V_{s'} = 43.2\text{mL}$), and for the HELIX fan-beam system, σ had a value of 1.75 mm (which leads to $V_{s'} = 38.8\text{mL}$).

Figure 2 shows one central section of the numerical phantom where the ROIs corresponding to the original striatum, the reference occipital region and the expanded striatum have been drawn.

Absolute quantification

The AQM was designed to provide an absolute volumetric activity at each voxel of the image. However, the values at each voxel of the reconstructed image (λ_i) obtained from Eq. 2 cannot be considered as real activity values. It is

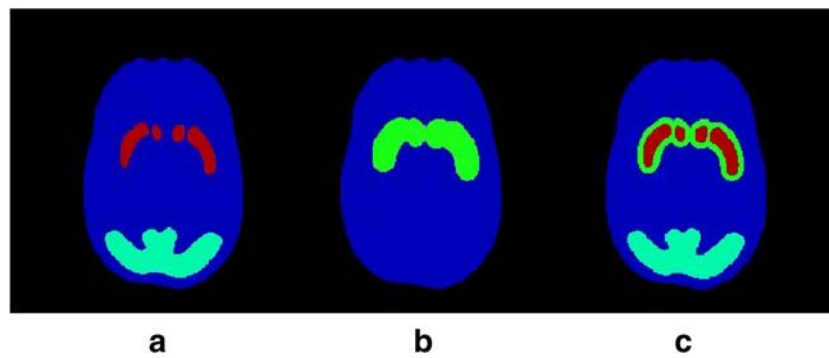


Fig. 2 A central slice of the phantom showing: **a** the considered ROIs for the striatal nuclei (*red*) and the occipital region (*light blue*), **b** the expanded striatal ROI (*green*) and **c** the overlay of **a** and **b**

therefore necessary to find a factor that transforms these calculated values into real activity. To calculate this factor, the reconstructed image at the first iteration is selected as the input activity distribution of the SimSET simulator. The number of detected counts obtained in this simulation is compared with the total counts of the original projections. The factor that matches the counts of the simulated and the original projections is finally applied to the reconstructed image.

Results

The high-energy contamination contribution

Figure 3 represents for each of the cameras studied the contribution of the primary, low-energy scattered photons

and high-energy scattered photons to the total projections. The images correspond to a noisy simulation of the striatal numerical phantom with a SUR value of 6. The numerical values of these contributions are also shown to emphasise the different contributions of the high-energy contamination when using two imaging systems equipped with a parallel and a fan-beam collimator and employing different acquisition protocols.

Relative quantification

To assess the effect of the corrections for the degrading phenomena in the quantification, results will be shown for different cases: (a) reconstruction without corrections (OSEM), (b) reconstruction with attenuation correction (OSEM-A), (c) 3D-reconstruction with attenuation and PSF corrections (OSEM-AP), (d) 3D-reconstruction with

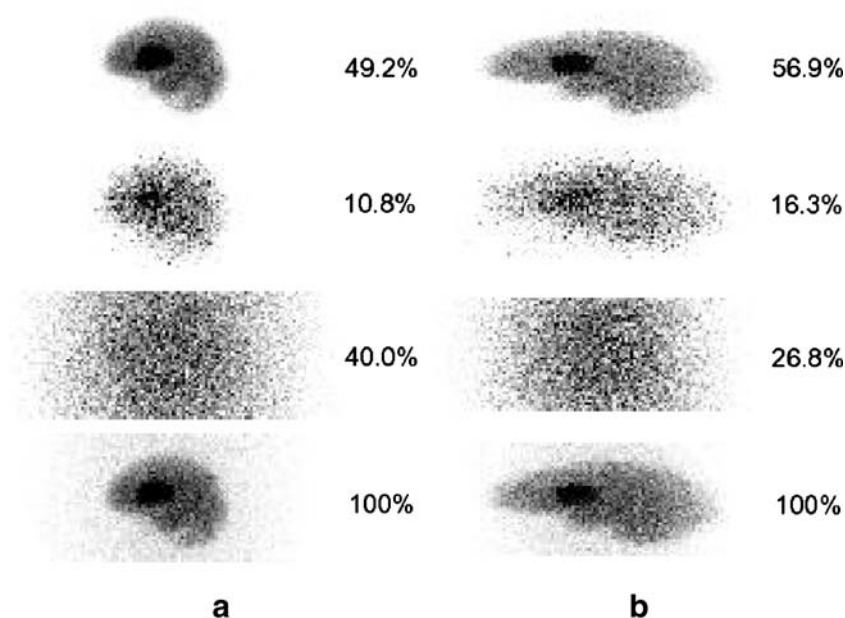


Fig. 3 A simulated projection of the striatal phantom with SUR of 6 for **a** the E.CAM system and **b** the HELIX system. From *top* to *bottom*: primary, low-energy scattered photons, high-energy scattered

photons and total photons detected. The numerical values of each contribution are also shown. Each image has been normalised to its maximum to improve its contrast

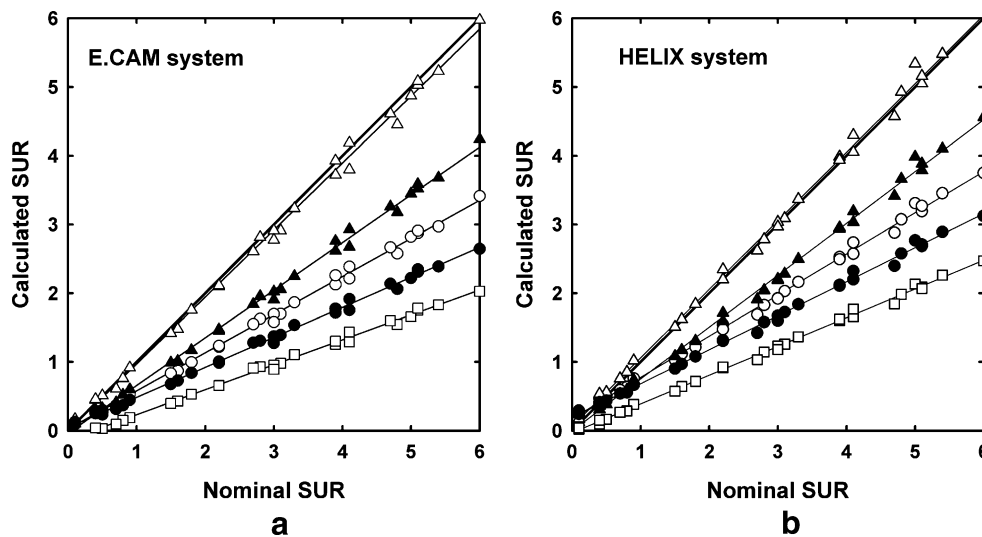


Fig. 4 Calculated SURs obtained with different corrections for **a** the E.CAM system and **b** the HELIX system: without corrections (OSEM) (empty squares), OSEM-A (filled circles), OSEM-AP (empty circles), OSEM-APS (filled triangles) and OSEM-APSV (empty triangles)

attenuation, PSF and scatter corrections (OSEM-APS) and (e) OSEM-APS plus PVE compensation (OSEM-APSV).

Figure 4 shows the calculated SURs against the nominal SURs for the 30 simulated studies and after reconstruction with different corrections. These values correspond to the eighth iteration for the E.CAM camera and to the sixth iteration for the HELIX camera. Fitting these plots to a straight line, we find correlation coefficients ranging from 0.997 to 0.998 for all the corrections applied, which demonstrates that there is a linear correlation between calculated and true values. This linear correlation may be described as:

$$SUR_{\text{calculated}} = \alpha SUR_{\text{theoretical}} + \beta \tag{6}$$

where α is the slope of the regression line and β stands for the intercept at the origin. The dark solid line in Figure 4 corresponds to the identity line, whereas the light solid lines correspond to the linear fits calculated for each correction. The PVE compensation was applied by expanding the original striatum volume from $V_s=21.5$ to a volume of $V_s = 43.2\text{mL}$ ($\Delta V=21.7$ mL) for the E.CAM system and from $V_s=21.5$ to $V_s = 38.8\text{mL}$ ($\Delta V=17.3$ mL) for the HELIX system.

Table 3 shows the mean and standard deviations for α and β , and the correlation coefficients of the linear fits for each acquisition system and for all the corrections implemented.

In Figure 5, we can observe the reconstructed image of a central slice at the first iteration of the reconstruction algorithm for two cases: OSEM-AP and OSEM-APS. The improvement in the image quality can be clearly noted when the scatter correction is included. The first iteration is the most suitable for visual assessment, although the most accurate quantification results are achieved at a higher number of iterations.

Absolute quantification

Figure 6 shows the bias between calculated and nominal mean activity concentration values as a function of nominal SUR. Quantification of the radiotracer uptake is less sensitive to PVE in the occipital region than in the striatum because of its size [31]. Therefore, PVE compensation is omitted for the occipital region and only the bias in the striatum after PVE compensation is reported.

Table 3 Mean and standard deviations for α and β and correlation coefficients of the linear fits

Correction level	α	β	r^2	Correction level	α	β	r^2
E.CAM system				HELIX system			
OSEM	0.36±0.00	-0.13±0.01	0.997	OSEM	0.42±0.00	-0.03±0.01	0.998
OSEM-A	0.44±0.00	0.05±0.02	0.997	OSEM-A	0.50±0.01	0.19±0.02	0.997
OSEM-AP	0.55±0.01	0.02±0.02	0.997	OSEM-AP	0.60±0.01	0.20±0.02	0.997
OSEM-APS	0.69±0.01	-0.03±0.02	0.997	OSEM-APS	0.75±0.01	-0.00±0.03	0.997
OSEM-APSV	0.97±0.01	-0.00±0.03	0.997	OSEM-APSV	1.00±0.01	0.06±0.03	0.997

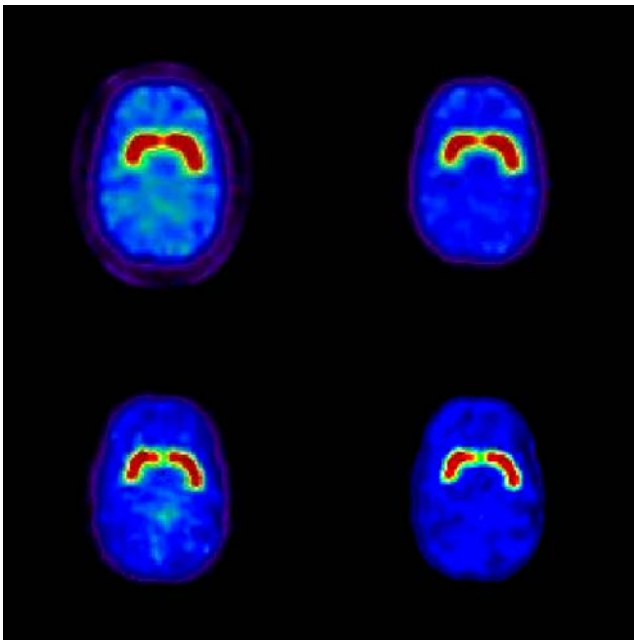


Fig. 5 Reconstructed central slice of the striatal brain phantom for the E.CAM system (*top*) and the HELIX system (*bottom*). For each camera, the images correspond to a nominal SUR of 4.7 and to a reconstruction using OSEM-AP (*left*) and OSEM-APS (*right*)

The bias in the striatum is shown when OSEM-APS and OSEM-APSV are used and in the occipital region when the OSEM-APS is applied. The bias from the true values was calculated as:

$$\bar{A}_{\text{bias}}(\%) = \frac{\bar{A}_{\text{calculated}} - \bar{A}_{\text{nominal}}}{\bar{A}_{\text{nominal}}} \times 100 \quad (7)$$

As can be observed in Fig. 6, for the HELIX system and for low values of SUR (approximately between 0.5 and 1), there is a slight positive bias in the striatum when PVE is compensated and a slight negative bias in the occipital region. This causes an overestimation of the calculated SUR in patients with severe reduction in the DAT density.

Discussion

Figure 3 highlights the importance of the high-energy contamination when pharmaceuticals labelled with ^{123}I are used in brain SPECT imaging. This contribution is strongly dependent on the acquisition system employed. When a LEHR parallel collimator is employed using the parameters shown in Table 1, more than 50% of the total photons is due to scattered photons. Indeed, high-energy photons account for 40%, which agrees with previous reported results [13] for the same imaging system. The high-energy photons degrade the image quality as they reduce the signal-to-noise ratio and the resolution in the projections. For the LEHR fan-beam collimator studied, the scattered

photons contribute up to 43%, whereas high-energy contamination contribution is about 27%.

The results in Fig. 4 and Table 3 demonstrate that the recovered SUR values have a linear correlation with the true specific ratios for both cameras and for each correction applied. It should be pointed out that the relationship between measured and true SUR values is mainly linear with a non-zero intercept at the origin. For high nominal SURs, the slope (α) of the linear regression determines the SUR recovery factor. Nevertheless, for low nominal SURs, the value of the intercept at the origin β becomes a determinant parameter as it induces a bias in the recovery factor.

The values of α shown in Table 3 indicate that although both imaging systems achieve different recovery factors with the same corrections, there is a continuous improvement as the corrections are progressively included. For both cameras, the results in Table 3 show that the successive corrections raise the value of α from 36 to 97% for the E.CAM system (total increase of 61%) and from 42 to 100% (total increase of 58%) for the HELIX system. For the E.CAM camera, the total increase of 61% corresponded to 8% for the attenuation correction, 11% for the PSF correction, 14% for the scatter correction and 28% for the PVE compensation. For the HELIX camera, the total increase of 58% corresponded to 8% for attenuation, 10% for PSF, 15% for scatter and 25% for PVE. These values demonstrate that PVE compensation plays a major role in the recovery of the true specific ratios as it may induce an improvement of approximately 25–30% in α values depending on the imaging system used. The scatter correction also plays an important part as it increases α values by 15%. PSF and attenuation corrections are the least significant corrections with improvements of around 10 and 8%, respectively.

For all the cases with the exception of OSEM-APSV, the HELIX camera shows a value of α that is, on average, 6% higher than that of the E.CAM camera. On the other hand, the two systems differed in the behaviour of the β values depending on the correction applied. One important fact is that scatter correction causes β to fall close to 0. The addition of the PVE compensation induces a slight increase in β , which has no relevance in the recovery factor of both cameras. Furthermore, the PVE compensation minimises the differences in α , so that both imaging systems attain a recovery factor of around 100%. Our study suggests that recoveries close to 100% may be obtained by expanding the original striatal ROI in 1σ of the spatial resolution of the reconstruction. Thus, the enlargement of the original ROI by 1σ may be established as a general criterion for PVE correction in dopaminergic SPECT studies.

Overall, all these results indicate that although the correction for attenuation is considered to be mandatory in the clinical routine [8], it is necessary to correct all the

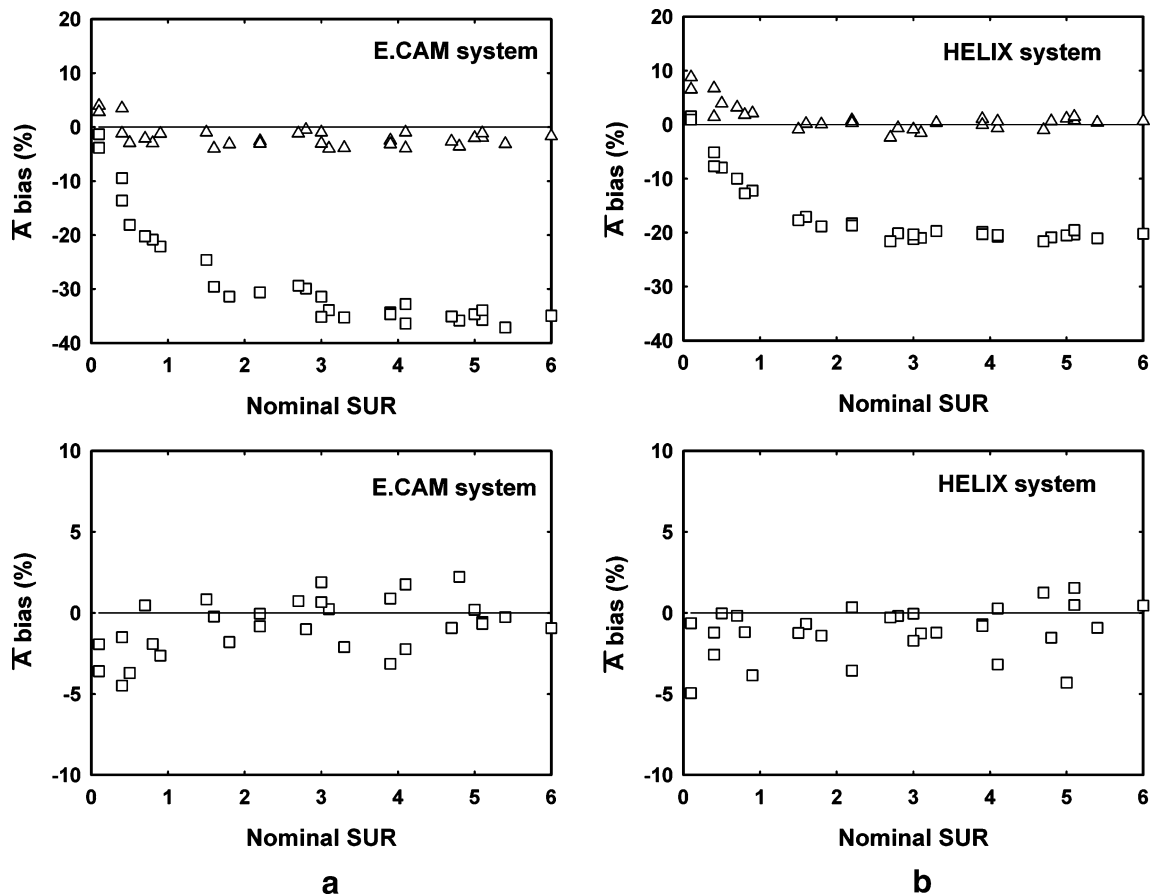


Fig. 6 The activity concentration bias (%) between calculated and nominal mean activity concentration values vs nominal SURs for (top) the striatum when OSEM-APS (empty squares) and OSEM-APSV (empty triangles) are used, and (bottom) the occipital region when

OSEM-APS is used (empty squares). Biases are shown for: **a** the E. CAM system and **b** HELIX system. Horizontal lines represent a percent bias equal to 0

image-degrading effects to achieve the nominal SURs. Thus, for a SUR of 4, the recovered SUR for the E.CAM system is 33% without corrections, 45% for OSEM-A, 56% for OSEM-AP, 68% for OSEM-APS and 97% for OSEM-APSV. For the HELIX system, the recovered SUR is 41% without corrections, 55% for OSEM-A, 65% for OSEM-AP, 75% for OSEM-APS and 102% for OSEM-APSV.

As the two gamma cameras equipped with completely distinct collimators and using different data acquisition protocols lead to similar SUR values when the AQM plus PVE compensation is employed, the proposed method may therefore be suitable for comparative studies using different gamma cameras or multicentric studies.

Furthermore, our results also highlight the importance of correcting for degradations to improve absolute quantification in neurotransmission SPECT studies with ¹²³I-labelled radioligands. In this regard, Fig. 6 shows that when the 3D reconstruction includes attenuation, PSF and scatter correction, the calculated mean activity concentration in the striatum is underestimated by about 35% for the E.CAM system and about 20% for the HELIX system, whereas the maximum percent bias in the occipital region is about 5%

for both cameras. PVE compensation proved to be effective in minimising the bias in the calculated mean activity concentration in the striatum, reducing errors to about 5% for both systems. These results indicate that PVE compensation in the striatum is necessary for absolute quantification. PVE compensation in the occipital region is not necessary as this area is large enough to influence the measurement of its mean activity concentration.

Conclusions

Our findings corroborate that quantitative results are dependent on the imaging system used in the acquisition when the reconstruction method does not include all the corrections for all the degrading phenomena [32, 33]. When all the corrections were incorporated into the quantification method, the differences practically disappeared, and both imaging systems reached approximately nominal values. The methodology presented in this paper establishes the corrections and the criteria to follow to compensate for all the image-degrading phenomena that affect neurotransmission ¹²³I SPECT imaging, including a PVE compensation.

We have sought to show that our quantification method leads to the theoretical quantitative values for two imaging devices equipped with different collimator systems and using different acquisition protocols.

Acknowledgements This work was supported in part by the IM3 network (Ministerio de Sanidad), with grants from the Fondo de Investigaciones Sanitarias del Instituto de Salud Carlos III projects G03/185, PI041017, PI050293 and Ministerio de Industria, Turismo y Comercio project CDTEAM (CENIT). D. Pareto was awarded a Beatriu de Pinós fellowship by the Departament d'Universitats, Recerca i Societat de la Generalitat de Catalunya.

References

1. Gelb DJ, Oliver E, Gilman S. Diagnosis criteria for Parkinson disease. *Arch Neurol* 1999;56:33–9.
2. Halldin C, Gulyas B, Langer O, Farde L. Brain radioligands—state of the art and new trends. *Q J Nucl Med* 2001;45:139–52.
3. Booij J, Tissingh G, Boer GJ, Speelman JD, Stoof JC, Janssen AGM, et al. [123I]FP-CIT SPECT shows a pronounced decline of striatal dopamine transporter labeling in early and advanced Parkinson's disease. *J Neurol Neurosurg Psychiatry* 1997;62:133–40.
4. Seibyl JP, Marek K, Sheff K, Baldwin RM, Zoghbi S, Zea-Ponce Y, et al. Test/retest reproducibility of iodine-123-β-CIT SPECT brain measurement of dopamine transporters in Parkinson's patients. *J Nucl Med* 1997;38:1453–9.
5. Linke R, Gostomzyk J, Hahn K, Tatsch K. [I-123] IPT-binding to the presynaptic dopamine transporter: variation of intra- and interobserver data evaluation in parkinsonian patients and controls. *Eur J Nucl Med* 2000;27:1809–12.
6. Catafau AM. Brain SPECT of dopaminergic neurotransmission: a new tool with proved clinical impact. *Nucl Med Commun* 2001;22:1059–60.
7. Stoof JC, Winogrodzka A, van Muiswinkel FL, Wolters EC, Voorn P, Groenewegen HJ, et al. Leads for the development of neuroprotective treatment in Parkinson's disease and brain imaging methods for estimating treatment efficacy. *Eur J Pharmacol* 1999;375:75–86.
8. Tatsch K, Asenbaum S, Bartebsstein P, Catafau A, Halldin C, Pillowsky LS, et al. European Association of Nuclear Medicine procedure guidelines for brain neurotransmission SPET using 123I-labelled dopamine transporter ligands. *Eur J Nucl Med* 2002; BP29:30–5.
9. El Fakhri G, Kijewski MF, Moore SC. Absolute activity quantitation from projections using an analytical approach: comparison with iterative methods in Tc-99m and I-123 brain SPECT. *IEEE Trans Nucl Sci* 2001;48:768–73.
10. Pareto D, Cot A, Pavia J, Falcón C, Juvells I, Lomeña F, et al. Iterative reconstruction with correction of the spatially variant fan-beam collimator response in neurotransmission SPET imaging. *Eur J Nucl Med Mol Imaging* 2003;30:1322–9.
11. Soret M, Koulibaly PM, Darcourt J, Hapdey S, Buvat I. Quantitative accuracy of dopaminergic neurotransmission imaging with 123I SPECT. *J Nucl Med* 2003;44:1184–93.
12. Cot A, Falcón C, Crespo C, Sempau J, Pareto D, Bullich S, et al. Absolute quantification in dopaminergic neurotransmission SPECT using a Monte Carlo-based scatter correction and fully 3-dimensional reconstruction. *J Nucl Med* 2005;46:1497–504.
13. Du Y, Tsui BMW, Frey E. Model-based compensation for quantitative 123I brain SPECT imaging. *Phys Med Biol* 2006;51:1269–82.
14. Beekman FJ, de Jong HWAM, Geloven S. Efficient fully 3-D iterative SPECT reconstruction with Monte Carlo-based scatter compensation. *IEEE Trans Med Imaging* 2002;21:867–77.
15. Zaidi H, Koral KF. Scatter modelling and compensation in emission tomography. *Eur J Nucl Med Mol Imaging* 2004;31:761–82.
16. Cot A, Sempau J, Pareto D, Bullich S, Pavia J, Calviño F, et al. Study of the point spread function (PSF) for 123I SPECT imaging using Monte Carlo simulation. *Phys Med Biol* 2004;49:3125–36.
17. Soret M, Alaoui J, Koulibaly PM, Darcourt J, Buvat I. Accuracy of partial volume effect correction in clinical molecular imaging of dopamine transporter using SPECT. *Nucl Instrum Methods A* 2007;571:173–6.
18. Rousset OG, Ma Y, Evans AC. Correction for partial volume effects in PET: principle and validation. *J Nucl Med* 1998;39:904–11.
19. Frouin V, Comtat C, Reilhac A, Grégoire MC. Correction of partial-volume effect for PET striatal imaging: fast implementation and study robustness. *J Nucl Med* 2002;43:1715–26.
20. Bullich S, Ros D, Pavia J, Penengo M, Mateos J, Falcon C, et al. Influence of coregistration algorithms on I-123-IBZM SPET imaging quantification. *Eur J Nucl Med Mol Imaging* 2004;31:S409.
21. Quarantelli M, Berkouk K, Prinster A, Landeau B, Svarer C, Balkay L, et al. Integrated software for the analysis of brain PET/SPECT studies with partial-volume-effect correction. *J Nucl Med* 2004;45:192–201.
22. Du Y, Tsui BMW, Frey EC. Partial volume effect compensation for quantitative brain SPECT imaging. *IEEE Trans Med Imaging* 2005;24:969–76.
23. Vanzi E, De Cristofaro M, Ramat S, Sotgia B, Mascalchi M, Formiconi AR. A direct ROI quantification method for inherent PVE correction: accuracy assessment in striatal SPECT measurements. *Eur J Nucl Med Mol Imaging* 2007;34:1480–9.
24. Harrison RL, Vannoy SD, Haynor DR, Gillispie SB, Kaplan MS, Lewellen TK. Preliminary experience with the photon history generator module of a public-domain simulation systems for emission tomography. In: 1993 records of IEEE Nuclear Science Symposium and Medical Imaging Conference, San Francisco, pp. 1154–8.
25. Pareto D, Cot A, Falcón C, Juvells I, Pavia J, Ros D. Geometrical response modelling in fan-beam collimators—a numerical simulation. *IEEE Trans Nucl Sci* 2002;49:17–24.
26. Cot A, Jané E, Sempau J, Falcón C, Bullich S, Pavia J, et al. Modeling of high-energy contamination in SPECT imaging using Monte Carlo simulation. *IEEE Trans Nucl Sci* 2006;53:198–203.
27. Hudson HM, Larkin RS. Accelerated image reconstruction using ordered subsets of projection data. *IEEE Trans Med Imaging* 1994;13:601–9.
28. Bowshe JE, Johnson WE, Turkington TG, Jaszczak RJ, Floyd CE, Coleman RE. Bayesian reconstruction and use of anatomical a priori information for emission tomography. *IEEE Trans Med Imaging* 1996;15:673–86.
29. Fleming JS, Bolt L, Stratford JS, Kemp PM. The specific uptake size index for quantifying radiopharmaceutical uptake. *Phys Med Biol* 2004;49:N227–34.
30. Tossici-Bolt L, Hoffmann SMA, Kemp PM, Mehta RL, Fleming JS. Quantification of [123I]FP-CIT SPECT brain images: an accurate technique for measurement of the specific binding ratio. *Eur J Nucl Med Mol Imaging* 2006;33:1491–9.
31. Du Y, Tsui BMW, Frey EC. Partial volume effect compensation for quantitative brain SPECT imaging. *IEEE Trans Med Imaging* 2005;24:969–76.
32. Koch W, Radau PE, Münzing W, Tatsch K. Cross-camera comparison of SPECT measurements of a 3-D anthropomorphic basal ganglia phantom. *Eur J Nucl Med Mol Imaging* 2006;33:495–502.
33. Koch W, Hamann C, Welsch J, Popperl G, Radau PE, Tatsch K. Is iterative reconstruction an alternative to filtered backprojection in routine processing of dopamine transporter SPECT studies? *J Nucl Med* 2005;46(11):1804–11.